

# WITNESSING THE FORMATION OF A GALAXY CLUSTER AT $Z = 0.485$ : OPTICAL AND X-RAY PROPERTIES OF RX J1117.4+0743 ([VMF 98] 097)<sup>1</sup>

E. R. CARRASCO<sup>2</sup>, E. S. CYPRIANO<sup>3</sup>, G. B. LIMA NETO<sup>4</sup>, H. CUEVAS<sup>5</sup>, L. SODRÉ JR.<sup>4</sup>, C. MENDES DE OLIVEIRA<sup>4</sup>, AND A. RAMIREZ<sup>5</sup>

The Astrophysical Journal *accepted*

## ABSTRACT

We present a multiwavelength study of the poor cluster RX J1117.4+0743 ([VMF 98] 097) at  $z=0.485$ , based on GMOS/Gemini South  $g'$ ,  $r'$  photometry and spectroscopy, and XMM-Newton observations. We examine its nature and surroundings by analyzing the projected galaxy distribution, the galaxy velocity distribution, the weak-lensing mass reconstruction, and the X-ray spectroscopy and imaging. The cluster shows a complex morphology. It is composed by at least two structures along the line-of-sight, with velocity dispersions of  $592 \pm 82 \text{ km s}^{-1}$  and  $391 \pm 85 \text{ km s}^{-1}$  respectively. Other structures are also detected in X-ray, in the galaxy projected number density map, and by weak-lensing. One of these clumps, located East from the cluster center, could be gravitationally bound and associated to the main cluster. The derived temperature and bolometric X-ray luminosities reveal that [VMF 98] 097 behave like a normal cluster, in agreement with  $L_X - T_X$  correlation found for both local ( $z = 0$ ) and moderate redshift ( $z \sim 0.4$ ) clusters. We find that the mass determination inferred from weak-lensing is in average 3 to 4.8 times higher (depending on the model assumed) than the X-ray mass. We have two possible explanations for this discrepancy: *i*) the cluster is in non-equilibrium, then the deviation of the X-ray estimated mass from the true value can be as high as a factor of two; *ii*) the intervening mass along the line-of-sight of the cluster is producing an over-estimation of the weak-lensing mass. Based on the analysis presented, we conclude that [VMF 98] 097 is a perturbed cluster with at least two substructures in velocity space and with other nearby structures at projected distances of about  $1 \text{ h}_{70}^{-1} \text{ Mpc}$ . This cluster is an example of a poor cluster caught in the process of accreting sub-structures to become a rich cluster.

*Subject headings:* galaxies: clusters: individual: RX J1117.4+0743 ([VMF 98] 097) - X-rays: galaxies: clusters - gravitational lensing - cosmology: observations - dark matter

## 1. INTRODUCTION

Cluster of galaxies are the largest gravitationally bound systems in the Universe. They are excellent laboratories for studying the large-scale structure formation, structure mass assembly and galaxy evolution. Numerical simulations show that massive clusters of galaxies form through hierarchical merging of smaller structures (e.g., West 1991; Richstone et al. 1992; Jenkins et al. 1998; Colberg et al. 1999). Clusters are complex systems, including a variety of interacting components such as galaxies, X-ray emitting gas and dark matter. Optical and X-ray studies show that a large fraction of clusters contains sub-structures, revealing that clusters are indeed dynamically active structures, accret-

ing galaxies and groups of galaxies from their neighborhoods (e.g. Lima Neto et al. 2003). Even though it is thought that rich clusters form at redshift 0.8–1.2 (or as high as 3.0, see Holden et al. 2004), there are numerous evidences (optical, X-ray) that clusters are still accreting sub-structures at intermediate and low redshifts (e.g., van Dokkum et al. 1998; Ferrari et al. 2005; Gonzalez et al. 2005). We may witness the assembly of rich clusters by observing large groups or poor clusters which, in turn, would be the future core of rich clusters. The details of this process will depend in part on how these large groups/poor clusters relate to more nearby structures.

Most galaxies in the Universe are concentrated in low-density environments (groups and poor clusters). For intermediate redshifts,  $z \sim 0.3$ –0.5, while massive clusters of galaxies have been widely studied, the intermediate-mass systems, those between loose groups and rich clusters of galaxies, have received comparatively little attention, either in X-rays or in the optical. In the context of the hierarchical structure formation scenario, an intermediate-mass system is a fundamental player to understand the process involved in the assembly of massive clusters of galaxies.

X-rays observations of intermediate-mass structures are particularly interesting, since the cluster X-ray faint-end luminosity function has eventually to turn over if the luminosity function of clusters is to meet that of single brightest elliptical galaxies with X-ray luminosities of a

<sup>1</sup> Based on observations obtained at the Gemini Observatory, which is operated by the Association of Universities for Research in Astronomy, Inc., under a cooperative agreement with the NSF on behalf of the Gemini partnership: the National Science Foundation (United States), the Particle Physics and Astronomy Research Council (United Kingdom), the National Research Council (Canada), CONICYT (Chile), the Australian Research Council (Australia), CNPq (Brazil) and CONICET (Argentina); Gemini program ID is GS-2003A-SV-206

<sup>2</sup> Gemini Observatory/AURA, Southern Operations Center, Casilla 603, La Serena, Chile

<sup>3</sup> Department of Physics and Astronomy, University College London, London WC1E 6BT, UK

<sup>4</sup> Departamento de Astronomia, Instituto de Astronomia, Geofísica e Ciências Atmosféricas, Universidade de São Paulo, Rua do Matão 1226, Cidade Universitária, 05508-090, São Paulo, Brazil

<sup>5</sup> Departamento de Física, Facultad de Ciencias, Universidad de La Serena, Benavente 980, La Serena, Chile

few  $10^{41}$  ergs  $s^{-1}$ . If this gap at intermediate luminosities could be closed, an X-ray luminosity function of all galactic systems could eventually be established, in analogy to that existing for the optical (Bahcall 1979). In addition, the spatial distribution of low-mass clusters at intermediate-redshifts could be studied in order to map regions just entering the non-linear regime, i.e.,  $\delta\rho/\rho \sim 1$ .

In the optical, the intermediate-mass systems are also of great importance and have received little attention. Many previous works have focused on the study of the galaxy population at intermediate redshifts but mostly in rich cluster of galaxies. These have established that the morphological content of galaxy clusters at intermediate redshift differs dramatically from that in nearby clusters (e.g., Dressler et al. 1997; Oemler et al. 1997; Smail et al. 1997). Indeed, at  $z \sim 0.3$ – $0.5$  there is an excess of spirals and a deficiency of lenticular galaxies in cluster cores when compared with the galaxy population in nearby clusters. It has been shown by these studies that the morphology-density relation is strong for concentrated, “regular” clusters, but nearly absent for clusters that are less concentrated and irregular, in contrast to the situation for low-redshift clusters, where a strong relation has been found for both. Dressler et al. (1997) suggests that these observations indicate that the morphological segregation proceeds hierarchically along the time, i.e. irregular clusters at intermediate redshifts are not old enough to present segregation. However, nearby irregular clusters seem to be evolved enough to establish the correlation. Taken together, these studies reveal that the morphological segregation has evolved significantly since  $z \sim 0.5$ , at least for regular clusters. However, it is not yet known at which degree, if any, morphological segregation evolves in the sparser environments of groups.

A few poor clusters or groups at intermediate redshifts have been studied, either in X-ray and/or in the optical (e.g., Ramela et al. 1999; Carlberg et al. 2001; Wilman et al. 2005; Mulchaey et al. 2006). One example is the work of Balogh et al. (2002), where it is presented the first spectroscopic survey of intrinsically low X-ray luminosity clusters ( $L_X < 4 \times 10^{43}$ ) at intermediate redshifts  $0.23 < z < 0.3$ . The ten systems studied have velocity dispersions in the range  $350$ – $850$  km  $s^{-1}$ , and are consistent with the local  $L_X$ – $\sigma$  correlation. They also find that the spectral and morphological properties of galaxies in these clusters are similar to those found in more massive systems at similar redshifts. More recently, Jeltama et al. (2006) described the properties of 6 intermediate redshift groups ( $0.2 < z < 0.6$ ) observed with XMM-Newton and concluded that they follow the same scaling relation observed in nearby groups.

In this paper we analyze the properties of the low-luminosity X-ray cluster of galaxies RX J1117.4+0743 – hereafter [VMF 98] 097 – based on optical and X-ray data. The cluster was selected from the 160 Square Degree ROSAT Cluster Survey (Vikhlinin et al. 1998) and is part of an ongoing project to study the cluster properties and the galaxy population of poor clusters in the redshift range  $0.15 < z < 0.5$ . This paper is arranged as follows. In Section 2 and 3 we describe the optical and X-ray data, respectively. Section 4 shows the results based on the analysis of these data: the velocity distribution, the galaxy projected distribution, the cluster color-magnitude diagram, a weak-lensing analy-

sis, and a study of the mass distribution, based on weak lensing and X-ray emission. In Sect. 5 we discuss the evolutionary status of [VMF 98] 097 and in section 6 we summarize our conclusions. Throughout this paper we adopt when necessary a standard cosmological model:  $H_0 = 70 h_{70}$  km  $s^{-1}$  Mpc $^{-1}$ ,  $\Omega_m = 0.3$  and  $\Omega_\Lambda = 0.7$ . At  $z = 0.485$ ,  $1''$  corresponds to  $6.0 h_{70}^{-1}$  kpc.

## 2. OPTICAL OBSERVATIONS AND DATA REDUCTION

This study is based on data collected with the Gemini Multi-Object Spectrograph (hereafter GMOS, Hook et al. 2004) at the Gemini South Telescope during the system verification process of the instrument.

### 2.1. Imaging

The cluster was imaged through the  $r'$  and  $g'$  Sloan filters (Fukugita et al. 1996) in 2003 March and May, using the detector array formed by three  $2048 \times 4608$  pixels EEV CCDs. With a pixel size of 13.5 microns and a scale of  $0''.073$  pixel $^{-1}$ , the detectors cover an area of  $5.5$  arcmin $^2$  on the sky. A total of 12 images of 600 sec in  $r'$  and 7 images of 900 sec in  $g'$  were obtained, giving an effective exposure time of 7200 seconds and 6300 sec in both filters, respectively. We adopted a  $2 \times 2$  binning for the images ( $0''.146$  pixel $^{-1}$  on the sky). Offsets between exposures were used to take into account the gaps between the CCDs (37 unbinned pixels) and for cosmic ray removal. All images were observed under good transparency (photometric) and seeing conditions, with seeing median values of  $0''.7$  and  $0''.8$  in  $r'$  and  $g'$ , respectively.

All observations were processed with the Gemini IRAF package v1.4 inside IRAF<sup>1</sup>. The images were bias/overcan-subtracted, trimmed and flat-fielded. The final processed images were registered to a common pixel position and then combined. The  $g'$  and  $r'$  magnitude zero-points were derived using Landolt (1992) standard stars observed immediately before and after the science exposures. The accuracy of the calibrations is of the order of 5% and 7% for  $r'$  and  $g'$ , respectively.

We have used SExtractor (Bertin & Arnouts 1996) to detect objects in the images and to obtain their relevant photometric parameters. The combined  $r'$  image was used to identify objects above a threshold of  $1\sigma_{\text{sky}}$  over the sky level ( $27.6$  mag/arcsec $^2$ ) and with at least 10 pixels ( $0.21$  arcsec $^2$ ). The photometry in the  $g'$ -band image was performed using the parameter ASSOC. This means that the photometric parameters in  $g'$  were obtained only for those objects detected in the  $r'$  image. The resulting catalog was then matched to obtain a final photometric catalog. We adopted the magnitude given by the parameter MAG\_AUTO as the value for the total magnitude of the objects. The colors of the objects were determined by measuring their magnitudes within a fixed 10 pixels diameter circular aperture ( $1''.5$ ), corresponding to  $9.0 h_{70}^{-1}$  kpc at the cluster rest-frame.

The SExtractor “stellarity” index (an indication of how certain an optical source is unresolved) was used to separate stars from galaxies. Objects with a stellarity index  $\leq 0.9$  were selected as galaxies. This cut is in agreement with a separate classification done by plotting pair

<sup>1</sup> IRAF is distributed by NOAO, which is operated by the Association of Universities for Research in Astronomy Inc., under cooperative agreement with the National Science Foundation.

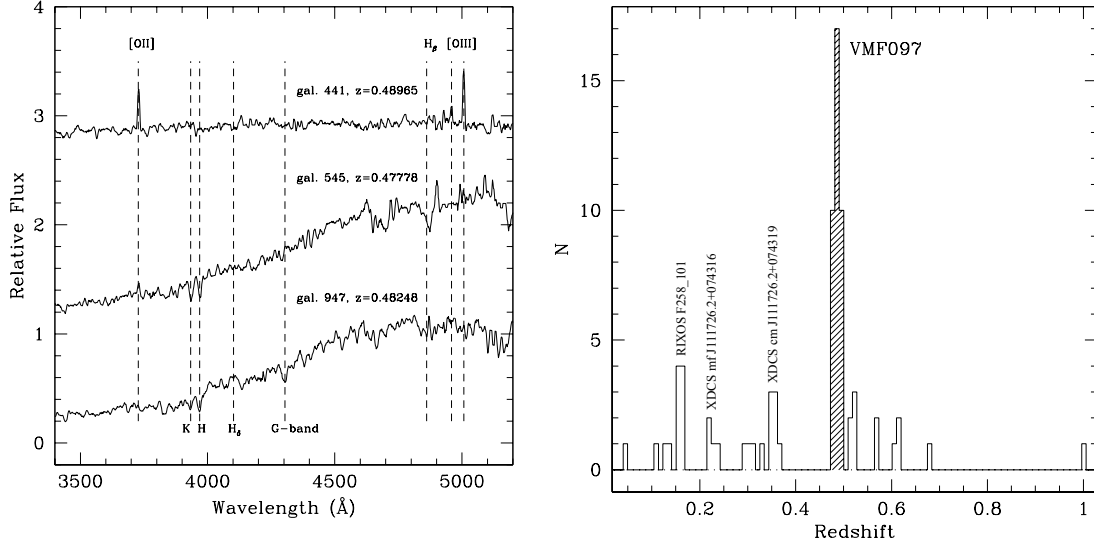


FIG. 1.— *Left*: Representative spectra of three galaxy members of the cluster. From top to bottom: late-type, intermediate-type and early-type. *Right*: Histogram of the redshift distribution of galaxies in the spectroscopic sample. The shaded histogram, centered at  $z \approx 0.485$ , shows the position of [VMF 98] 097 in the redshift space. Other foreground structures are also shown.

of object parameters, like central intensity *vs.* area, central intensity *vs.* size, and peak intensity *vs.* size, as well as by visual control. In all cases the classifications are consistent down to  $r' = 25.5$  mag. The galaxy counts calculated using the objects classified as galaxies reach their maximum at  $r' = 25.8$  mag. Using this information and the uncertainties in the galaxy classification above  $r' = 25.5$  mag, we have adopted this latter value as our limiting magnitude. The final catalog contains the total magnitudes, the colors and the structural parameters for 2698 objects classified as galaxies. Of these, 1348 are brighter than 25.5 mag in  $r'$  ( $M_{r'} = -16.7$  at the distance of the cluster).

## 2.2. Spectroscopy

The targets for spectroscopic follow up were selected based on their magnitudes only. No color selection was applied, meaning that the sample includes galaxies of different morphological types. All galaxies with apparent magnitudes brighter than  $r' = 23$  mag were selected for spectroscopy (31% of the total sample). Of these, only 79 objects were observed spectroscopically. Two masks were created: one for bright objects ( $r' \leq 20$  mag) and another for faint objects ( $20 < r' \leq 23$  mag).

The spectra of the galaxies were obtained with GMOS in 2003 May 29–30, during dark time, with a good transparency, and with a seeing that varied between 0".8 and 0".9. A total exposure times of 3600 seconds and 6000 seconds were used for masks containing bright and faint objects, respectively. Small offsets of  $\sim 50$  pixels in the spectral direction ( $\sim 35$  Å) towards the blue and/or the red were applied between exposures to allow for the gaps between CCDs and to avoid any loss of important emission/absorption lines present in the spectra. Spectroscopic dome flats and comparison lamp (CuAr) spectra were taken after each science exposure. All spectra were acquired using the 400 lines/mm ruling density grating (R400) centered at 6700 Å, in order to maximize the wavelength coverage for galaxies at the cluster distance.

All science exposures, comparison lamps and spectroscopic flats were bias subtracted and trimmed. Spec-

troscopic flats were processed by removing the calibration unit plus GMOS spectral response and the calibration unit uneven illumination, normalizing and leaving only the pixel-to-pixel variations and the fringing. The resulting 2-D spectra were then wavelength calibrated, corrected by S-shape distortions, sky-subtracted and extracted to an one-dimensional format using a fixed aperture of 1".3. The residual values in the wavelength solution for 20–30 points using a 4th or 5th-order Chebyshev polynomial typically yielded *rms* values of  $\sim 0.15$ – $0.20$  Å. With the choice of a 0".75 slit width, the final spectra have a resolution of  $\sim 5.5$  Å (measured from the arc lines FWHM) with a dispersion of  $\sim 1.37$  Å pixel<sup>-1</sup>, covering a wavelength interval of  $\sim 4400$ – $9800$  Å (the wavelength coverage depends on the position of the slit in the GMOS field-of-view). Finally, the residuals of the 5577 Å, 5890 Å, and 6300 Å night-sky lines were removed from all spectra using a 10-th order cubic spline polynomial. Beyond 7800 Å, the residuals of night-sky lines were simply masked.

To obtain the galaxy radial velocities, we first inspected the spectra to search for obvious absorption and/or emission features characteristic of early- and late-type galaxy populations. For galaxies with clear emission lines, the routine RVIDLINE in the IRAF RV package was used employing a line-by-line gaussian fit to measure the radial velocity. The residual of the average velocity shifts of all measurements were used to estimate the errors. For early-type galaxies, the observed spectra were cross-correlated with high signal-to-noise templates using the FXCOR program in the RV package inside IRAF. The errors given by FXCOR were estimated using the *r* statistic of Tonry & Davis (1979):  $\sigma_v = (3/8)(w/(1+r))$ , where  $w$  is the FWHM of the correlation peak and  $r$  is the ratio of the correlation peak height to the amplitude of the antisymmetric noise. The left panel in Fig. 1 shows the smoothed spectra of three galaxies identified as cluster members, corresponding to three different spectral types: early-type (bottom), late-type (top) and intermediate-type (middle).

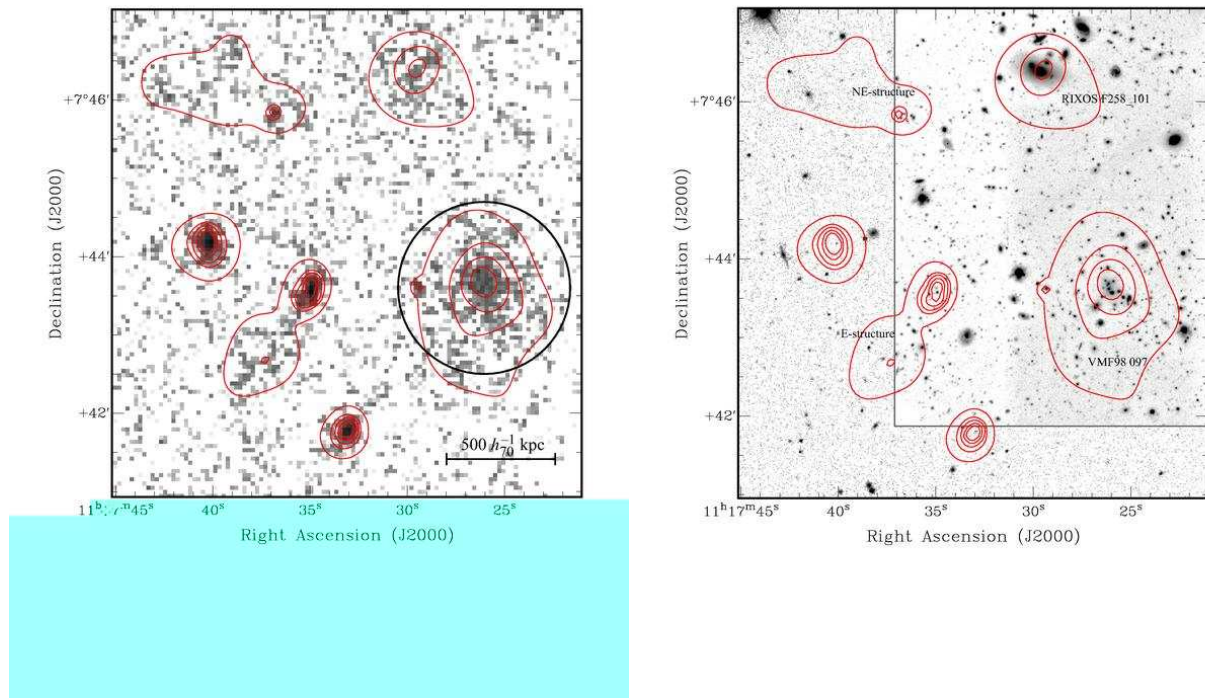


FIG. 2.— *Left*: Composite image using all EPIC MOS observations where the cluster is seen entirely, in the 0.3–8.0 keV band. The circle with 66'' radius shows the region where the [VMF 98] 097 spectrum was extracted (the scale length in the plot assumes  $z = 0.485$ ). *Right*: adaptively smoothed X-ray emission plotted over the GMOS  $r'$  plus SDSS  $r'$  composite image. The inner rectangle shows part of the region covered by the GMOS field. The thin lines in the figures are the isocontours at 0.4, 1.2, 2.0, 3.7, and 6.3  $\sigma$  above the X-ray background.

We were able to measure redshifts for 77 objects ( $\sim 95\%$  success rate). Seventy five of them are galaxies and two are M-class stars. As expected, the fraction of emission-line galaxies is relatively high and constitute 33% of the total sample. However, the fraction of emission-line galaxies that are cluster members is lower and represent only  $\sim 22\%$  of the cluster galaxy population. The emission-line galaxy fraction is in agreement with the results obtained by Balogh et al. (2002) for 10 intrinsically low X-ray luminosity cluster ( $L_X < 4 \times 10^{43} \text{ erg s}^{-1}$ ) at  $z \sim 0.25$  (see section 4.1 for more details). The measured redshifts, corrected to the heliocentric reference frame, and the corresponding errors are listed in Table 1 (columns 6 and 7, respectively). The galaxy identifications and their sky coordinates are given in the first 3 columns. The apparent total magnitudes in  $r'$ -band and the  $g' - r'$  colors inside a fixed circular aperture of  $1''.5$  are listed in columns 4 and 5, respectively. The  $R$  value (Tonry & Davis 1979) listed in column 8 was used as a reliability factor of the quality of the measured velocity. For  $R > 3.5$ , the resulting velocity was that associated to the template which produced the lowest error. For galaxies with  $R < 3.5$ , we looked for absorption features like CaII and G-band in the spectra, and performed a line-by-line Gaussian fit using the package RVIDLINE. The resulting values were then compared with the velocities given by cross-correlation. In all cases the agreement between the two procedures were good.

The histogram of the redshift distribution is presented in the right panel of Fig. 1. The concentration of galaxies at  $z \approx 0.485$  (shaded area) indicates the position of the [VMF 98] 097 cluster. The peak at  $z \approx 0.16$  corresponds

to a group of galaxies, RIXOS F258\_101, located  $\sim 2'.5$  North of the cluster core (see Section 4.2). Two other small peaks can be seen which are probably related to the groups reported by Gilbank et al. (2004).

### 3. X-RAY OBSERVATIONS AND DATA REDUCTION

The cluster [VMF 98] 097 was serendipitously discovered in X-rays in a pointed ROSAT PSPC observation of QSO PG1115+080 (Vikhlinin et al. 1998). This object was observed by XMM-Newton in December 2002 (obsID 082340101) and twice in June 2004 (obsID 203560201 and 203560401). [VMF 98] 097 is found in the field of view of the MOS1 in all exposures, but it was observed entirely by the PN detector only in the 2002 observation (only half of the cluster appears in any MOS2 field of view). This cluster was also observed by Chandra ACIS-I3 in June 2000 (P.I. G.P. Garmire) in a 26 ks exposure. However, it produced only  $\sim 200$  net counts (background corrected). Therefore, the Chandra observations are not used in the analysis.

We have downloaded the ODF files from XMM public archives and performed the MOS and PN “pipelines”, which consist in the removal of bad pixels, electronic noise and correction for charge transfer losses with the program SAS v6.5.0. We have then applied the standard filters and removed the observation times with flares using the light-curve of the [8.0–14.0 keV] energy band. The final exposure times after subtracting high particle background intervals of the cleaned event files for all observation are given in Table 1 together with the net count number (i.e., source minus background counts).

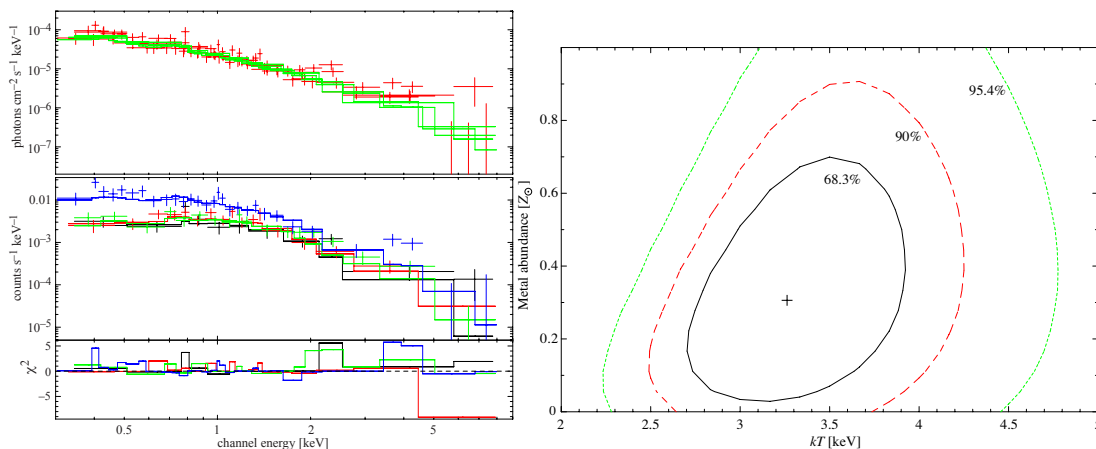


FIG. 3.— *Left*: Best fit MEKAL model. Top: data from MOS1 and PN and the best fit spectrum in units of photons  $\text{cm}^{-2} \text{s}^{-1} \text{keV}^{-1}$ , corrected for instrumental effects; Middle, flux in counts  $\text{s}^{-1} \text{keV}^{-1}$ . The upper line corresponds to the PN data, the three MOS1 observations are seen below. Bottom: residuals of the best fit spectrum. *Right*: Correlation between temperature and metallicity obtained with the spectral fit. The contours correspond to 68.3%, 90%, and 95.4% confidence levels; the best-fitted value is shown with a plus sign.

### 3.1. X-ray Imaging and Spectroscopy

For the spectral analysis we have selected a circular region of  $1'1''$  centered at RA =  $11^{\text{h}}17^{\text{m}}26^{\text{s}}.5$ , DEC =  $+07^{\circ}43'33''$  (J2000). The background was selected in the same observation. We have used a larger extraction region near the detector border (this because [VMF 98] 097 is itself near the border), without any visible sources.

Since about half of the cluster falls outside the MOS2 field of view, we have used only MOS1 and PN cameras of the 2002 observations, and only the MOS1 of the 2004 observations. The total source counts, background subtracted, are also given in Table 1. The left panel of Figure 2 shows the composite image made with MOS1 and PN available data in the 0.3–8.0 keV band. The EPIC-MOS has a FWHM  $\approx 5''$  at the center of the detector. However the MOS point spread function has somewhat extended wings and the half energy width (HEW) is  $\approx 14''^2$ . For off-axis sources there is a degradation in the resolution, which also depends on the energy (Ehle et al. 2006). The cluster [VMF 98] 097 is located  $\approx 12'.5$  from the detector axis. Therefore the resolution at 1.5 keV is  $5'.5$  and  $6'.5$  for the MOS-1 and PN respectively. At 5 keV the resolution is  $6'.3$  and  $7'.6$  for the MOS-1 and PN respectively. The effective exposure time is also affected, but it is taken into account by the Redistribution Matrix File (RMF) and the Auxiliary Response File (ARF) (Ehle et al. 2006).

We also present in the right panel of Fig. 2 the smoothed X-ray emission plotted over the GMOS  $r'$  image. The core of the cluster, about  $1'$  South of the center of the image, is clearly detected in X-rays. The emission at the North of the image is associated with a foreground group at  $z \sim 0.16$  (see Section 4.2). Two other X-ray emission features are worth mentioning since they are also present in the galaxy-density map and in the weak-lensing map discussed below: the feature at the East of the cluster core (hereafter E-structure) and another at the Northeast, at the border of the optical image (hereafter the NE-structure).

The ancillary and redistribution files (ARF and RMF) were created with the SAS tasks `arfgen` and `rmfgen`,

taking into account the extended nature of the source. The MOS and PN spectra were fitted simultaneously, each spectrum with its own RMF, ARF, and background files. The spectral fits were done with XSPEC 11.3 in the range [0.3–8.0 keV] on the re-binned spectrum, with at least 12 counts per energy bin.

We have used the MEKAL (Kaastra & Mewe 1993; Liedahl et al. 1995) plasma model with a photoelectric absorption given by Balucinska-Church & McCammon (1992). For the hydrogen column density, we have adopted the galactic value at the position of [VMF 98] 097,  $N_{\text{H}} = 3.37 \times 10^{20} \text{cm}^{-2}$  (using the task `nh` from FTOOLS, which is an interpolation from the Dickey & Lockman 1990, galactic  $N_{\text{H}}$  table).

Given the evidences presented in Sect. 4.1 that the velocity distribution has two peaks, we have tried the spectral fits with different redshifts but the results are virtually the same: we cannot, with these spectra, obtain a redshift estimate of the source. We have also tried a two component MEKAL model, representing each source in the line-of-sight; however the fit did not converge because of the low signal-to-noise ratio of the spectra. Therefore, we give our results here as mean emission-weighted values, adopting a fixed mean redshift.

The best-fit model is shown in the left panel of Fig. 3. Fixing the redshift at  $z = 0.485$  (average redshift obtained for the cluster, see below), we obtain the following temperature and metal abundance (metallicity):  $kT = 3.3_{-0.6}^{+0.7} \text{keV}$  and  $Z = 0.3_{-0.2}^{+0.4}$  (the errors are at the 90% confidence levels). The fit is fairly good with  $\chi^2/\text{d.o.f.} = 247.0/250$  (the null hypothesis probability is 0.54).

The metallicity is not well constrained since the Fe-K line is not well detected. This is also shown in the temperature-metallicity correlation plot, in the right panel of Fig. 3.

#### 3.1.1. Measured flux and luminosity

We have computed the unabsorbed X-ray flux and luminosity in different energy bands using the plasma model described in the previous section. Table 1 summarizes these results.

With the determined temperature and bolometric luminosity, [VMF 98] 097 is found to behave like a nor-

<sup>2</sup> see [http://xmm.vilspa.esa.es/external/xmm-user\\_support/documentation/uhb/index.html](http://xmm.vilspa.esa.es/external/xmm-user_support/documentation/uhb/index.html)



mal cluster, in agreement with the local  $L_X$ – $T_X$  correlation (Willis et al. 2005) and the correlation for intermediate redshift clusters ( $z \sim 0.4$ , Jelte et al. 2006). The agreement with both local and intermediate relations comes from the intrinsic scatter in both relations and the error bars in our cluster. Therefore, the X-ray emission of [VMF 98] 097 is not affected (at least significantly) by the emission from the group/structure behind the cluster.

### 3.1.2. Radio emission

A search with NED<sup>3</sup> reveals that this cluster has a radio emission at 1.4 GHz associated to it. We have used this information to look for a radio image in the FIRST survey<sup>4</sup>. The radio image has a FWHM of  $5''.4$  and the radio emission contours are shown in Fig. 4.

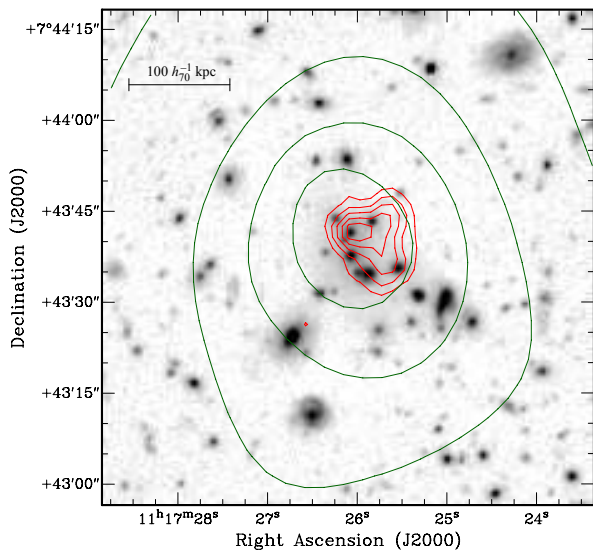


FIG. 4.— GMOS optical image with VLA 1.4 GHz continuum emission isocontours (central, thick lines) and X-ray emission contours (thin lines) overlaid. The radio contours are linearly spaced in intensity. The X-ray contours are the same as in Fig. 2. Notice the wide-angle tail morphology of the radio emission.

The peak of the radio emission coincides with galaxy 1098 (Tab. 1) and the center of the X-ray emission. It has wide-angle tail morphology, which is often found in radio galaxies in the center of clusters (Roettiger et al. 1996; Gomez et al. 1997). This radio morphology implies that the radio galaxy is moving with respect to the ICM. This could be due to the bulk motion of the intra-cluster gas (Burns et al. 2002), for instance, because of a cluster or group merging. In the present case, based on the broadening of the radio emission, the direction of motion perpendicular to the line-of-sight is West–East.

The presence of an AGN may contaminate the X-ray spectrum with a hard component, making the spectral determined temperature artificially higher. The radio emission associated with galaxy 1098 suggests such an AGN. However, there is no sign in either XMM or Chandra data suggesting a point source or an excess X-ray emission at the spatial location of galaxy 1098. Since

the X-ray surface brightness is quite flat in the cluster center, a bright X-ray AGN would be detectable. In addition, there is no indication of an AGN in the optical spectrum of the galaxy 1098.

## 4. OPTICAL DATA ANALYSIS

### 4.1. Velocity distribution

Thirty seven out of 75 galaxies with measured velocities are located in the redshift interval  $0.47 < z < 0.50$ , corresponding to the prominent peak seen in the right panel of Fig. 1. The velocity distribution of these galaxies is shown in Fig. 5. It is clear, from the figure, the complexity of the cluster. In order to investigate its structure, we use the KMM test (Ashman, Bird & Zepf 1994), which is appropriate to detect the presence of two or more components in an observational data set.

First we consider whether the data is consistent with a single component. The results of applying the test in the homoscedastic mode (common covariance) yields strong evidence that the redshift distribution of galaxies in the redshift interval above is at least bimodal, rejecting a single Gaussian model at a confidence level of 97.7% (P-value of 0.024). The P-value is another way to express the statistical significance of the test, and is the probability that a likelihood test statistic would be at least as large as the observed value if the null hypothesis (one component in this case) were true. Assuming two components, they are located at  $z = 0.482$  and  $z = 0.494$ , corresponding to the structures S1 and S2 in Figure 5. They are separated by  $3000 \text{ km s}^{-1}$  in the cluster rest frame.

The histogram shows another gap of  $\sim 2000 \text{ km s}^{-1}$  (also in the cluster rest frame) between S2 and S3 which is formed by 4 galaxies in the interval  $0.496 < z < 0.510$ . If we assume that the velocity distribution in Figure 5 is indeed tri-modal, the KMM test rejects a single Gaussian at a confidence level of 99% (P-value of 0.010). Consequently, a model with three components is statistically more significant than a model with two components. In this case, the procedure assigns a mean value of  $z = 0.482$ ,  $z = 0.491$  and  $z = 0.498$  with 23 (62%), 10 (27%) and 4 (11%) galaxies for each of the structures, respectively.

We used the robust bi-weight estimators  $C_{BI}$  and  $S_{BI}$  of Beers et al. (1990) to calculate a reliable value for the average redshifts (central location) and the velocity dispersions (scale) of the two main velocity structures (S1 and S2) present in the cluster. We used an iterative procedure by calculating the location and scale using the ROSTAT program and applying a  $3\sigma$  clipping algorithm to the results. We repeated this procedure until the velocity dispersion converged to a constant value. The best estimates of the location and scale for S1 and S2 are shown in Table 1 (columns 5 and 6 respectively). The table also shows, for the velocity structure S1, the virial radius  $R_v$  and the virial mass (column 8), computed with the prescription of Heisler et al. (1985). The velocity structure S2 is not centrally concentrated and is probably not virialized (see below). We then chose to not determine its  $R_v$  and virial mass. The number of galaxies in the structure at  $z = 0.49804$  (S3, see Fig. 5) is too small for a reliable determination of the velocity dispersion and other dynamical parameters (Beers et al. 1990).

<sup>3</sup> NASA/IPAC Extragalactic Database, <http://nedwww.ipac.caltech.edu/>

<sup>4</sup> Faint Images of the Radio Sky at Twenty-centimeters, <http://sundog.stsci.edu/>

It is worth noting that the derived line-of-sight velocity dispersion for S1 of  $592 \pm 82 \text{ km s}^{-1}$  agrees well (inside the 68% confidence interval) with the value inferred from the intra-cluster medium temperature. Indeed, using the  $T_X$ - $\sigma$  relation from Xue & Wu (2000) (which is derived from a local sample) the measured X-ray temperature of  $kT = 3.3^{+0.7}_{-0.6} \text{ keV}$  implies  $\sigma = 672^{+57}_{-53} \text{ km s}^{-1}$ . This result suggests that the X-ray emission is associated to S1. This seems to be the case since the X-ray emission is centered on the cluster core, which is associated with the velocity structure S1.

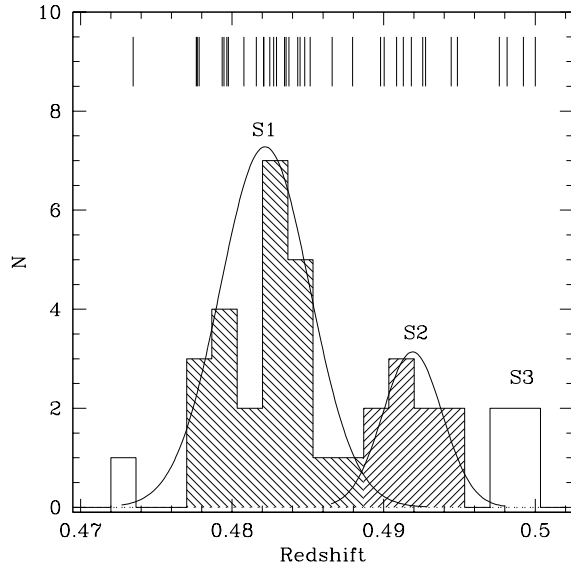


FIG. 5.— Histogram of the redshift distribution of 37 galaxies in area of [VMF 98] 097. The two main structures (S1 and S2) are clearly seen in the plot. A third structure, with 4 galaxies located at  $z > 0.492$ , is also shown in the figure.

#### 4.2. Galaxy projected distribution

Figure 6 shows an adaptive-kernel density map (see Silverman 1986) based on a sample of 272 galaxies brighter than  $r' = 23 \text{ mag}$ . The area corresponds roughly to  $\sim 2 \times 2 h_{70}^{-2} \text{ Mpc}^2$  at the rest-frame of the cluster. All structures shown in this map are above the  $3 \sigma$  significance level.

Most of the structures identified in this figure are also present in the X-ray map (Figure 2). The [VMF 98] 097 cluster is represented by the high density region located  $\sim 1'$  South from the center of the image. The second highest density region, located at the top of the figure, corresponds to a foreground group at  $z \approx 0.16$  (RIXOS F258\_101; Mason et al. 2000). A third structure, located  $\sim 2'$  East from the cluster core, is the E-structure present in the X-ray map.

Most galaxies in the cluster core have velocities in the range of S1 (squares), however the galaxies in S2 (rhombi) are mainly distributed, without any significant concentration, to the South of the cluster core. We have velocities for only four objects which overlap in space with the E-structure: one is in S1, another in S2 and two others corresponding to a nearby and to a background object. The detection of two velocities at the cluster

redshift, as well as the X-ray emission, suggests that the E-structure is probably dynamically associated with the cluster.

Figure 6 shows also two overdensities NE from the cluster center. The first one, at  $\sim 1'$ , may be associated to the cluster (a substructure), since several velocities in the region are in the redshift of the cluster core. The second, at  $\sim 2'$ , is the NE-structure in the X-ray map, and may be either a substructure or a background cluster (the galaxies there tend to be fainter than those in the cluster core). Unfortunately we do not have any radial velocity in this region to confirm this point.

As shown below, the weak-lensing analysis also detect most of the features present in Figure 6.

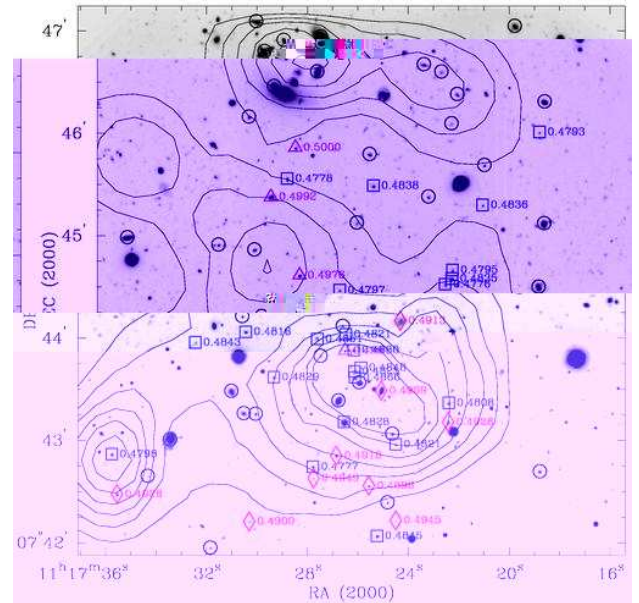


FIG. 6.— The projected galaxy density map of 272 galaxies brighter than  $r' = 23 \text{ mag}$ . The adaptive kernel density map is superimposed on the  $g'$  band image ( $5.37 \times 5.37 \text{ arcmin}^2$ ). The cluster is located  $\sim 1'$  southward from the center of the image. A second structure, located towards the NE from the cluster core, seems to be also associated with [VMF 98] 097. The symbols in the plot represent all galaxies with measured velocities. The squares and rhombi represent the member galaxies of S1 and S2 structures, respectively. The four triangles represent the member galaxies of S3. The circles indicate the background and foreground galaxies.

#### 4.3. The color-magnitude diagram

Galaxy colors provide valuable information about the stellar content of galaxies, allowing to identify passive and star-forming galaxies in clusters. Fig. 7(a) shows the color-magnitude diagram (CMD) for all galaxies detected in the images. Colors and the total magnitudes have been corrected by galactic extinction from the reddening maps of Schlegel et. al (1998) and using the relations of Cardelli et. al. (1989) ( $A_g = 0.15 \text{ mag}$  and  $A_r = 0.12 \text{ mag}$ , respectively).

An inspection of this CMD shows that the galaxy populations of the two main structures of the cluster are not the same, with S1 containing much more red galaxies (at the so-called cluster red sequence in  $(g' - r')_0 \approx 1.9$ ) than S2 and S3. This behavior is better seen in the color distribution histogram of galaxies with measured velocities. Fig. 7(b) indicates that S1 is dominated by a red galaxy

population (right shaded histogram), while S2 and S3 contains mostly blue galaxies (left shaded histogram). It is important to note also that S2 and S3 are formed by galaxies that, in average, are  $\sim 0.3$  fainter than those in S1.

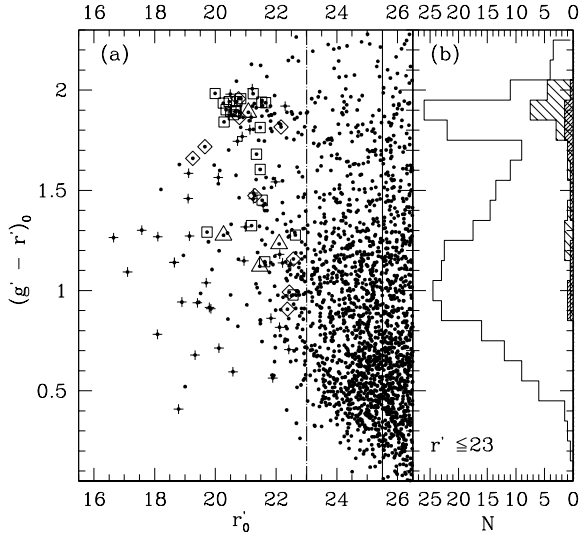


FIG. 7.— (a) Color-magnitude diagram for all galaxies detected in the images. Colors and magnitude are corrected for galactic extinction (see text). The symbols are the same as in Fig. 6 (see Sect. 4.2). The solid line indicates the magnitude of the sample completeness ( $r' = 25.5$  mag). The dashed-dotted line represents the limit imposed to select galaxies for the spectroscopic observations ( $r' = 23$ ). (b) Open histogram: color distribution of 272 galaxies with  $r' \leq 23$ ; Shaded histograms: color distribution of the galaxies members of S1 (shaded to the right) and S2+S3 (shaded to the left) structures.

In a cluster that is dynamically active, it is expected to find a high fraction of star-forming galaxies. The results shown above point into that direction. As we mentioned in section 2.2, the average fraction of emission-line galaxies in the cluster is relatively small and constitute only 22% of the population. However, there are differences in the content of the galaxy population in the structures. In S1, only 17% of the galaxies (4 out of 23) are emission-line objects. In the case of S2 and S3, the fraction is much higher, and constitute 31% of the population (5 out of 13). The results agree well with what we see in the color-magnitude diagram: the emission-line, star-forming (blue) galaxies are more numerous in S2 and S3 than in S1.

We investigated the median magnitudes and colors for all galaxies with  $r' \leq 23$  in the two overdensities detected in X-ray, with the density map (E-structure and NE-structure), and in the cluster core. For the analysis we select the galaxies inside a radius of  $20''$  ( $\sim 0.12 h_{70}^{-1}$  Mpc at the cluster distance) from the center given by the maximum of the galaxy overdensity (see Fig. 6). Table 1 summarizes the median magnitudes and colors for the three overdensities.

The galaxies in the E-structure are  $\sim 1$  magnitude fainter and slightly bluer than the galaxies in the cluster core. The E-structure contains two galaxies with veloc-

ities at the cluster redshift. One of them is a member of S1, with  $(g' - r') = 1.92$ . The other is a member of S2, with  $(g' - r') = 1.47$ , similar to the median color value derived for this structure. The E-structure is also detected in X-rays and in the weak-lensing mass map.

The galaxies in the NE-structure are fainter and bluer than in the cluster core. This structure is detected in X-ray (Fig. 2), and also by weak lensing (see section 4.5.1). Due to the lack of redshift information in this region, we can only speculate about the nature of this structure, i.e., if it is a background or foreground cluster or even a sub-structure of [VMF 98] 097.

If the NE-structure is a background cluster, then one would expect a much fainter galaxy population, but with much redder colors. This is not the case, since the galaxies in this region are faint, but bluer than in the core of [VMF 98] 097. Another possibility is that it is indeed a background cluster of blue, star-forming galaxies, where the red sequence is not yet established. Finally, this structure could be associated to the foreground group RIXOS F258\_101 at  $z \approx 0.16$  (the NE-structure is located at  $1/7$  from the center of this group). However this is very unlikely. The average magnitude of the galaxies in the group is  $\sim 18.8$  mag with a median color of  $(g' - r') = 1.2$ . Although the median color obtained for the NE-structure is similar to the median color of the galaxies in RIXOS F258\_101, the galaxy population is much fainter (3.5 mag).

#### 4.4. Weak Gravitational Lensing Analysis

Gravitational lensing is a powerful tool for studying the matter distribution in galaxy clusters. In its weak regime gravitational lensing allows the reconstruction of the projected mass distribution through the analysis of the small morphological distortions induced by gravitational lensing of background sources (weak shear field). This technique is completely independent of the dynamical state of the cluster. In this section we apply a weak-lensing analysis to the imaging data to estimate the mass distribution on the field of [VMF 98] 097.

##### 4.4.1. Galaxy shape measurements

The determination of the shapes of faint, putative background galaxies, was performed using the method described in Cypriano et al. (2004, 2005). In the following paragraphs we summarize the main steps of the procedure used in the analysis.

We performed galaxy shape measurements, including the removal of seeing effects and PSF anisotropies, using the algorithm IM2SHAPE (Bridle et al. 2002). This program models an astronomical object as a sum of Gaussian functions with an elliptical base and carries out the deconvolution of the object image with a local PSF extracted from the image itself. While stars were modeled as one simple Gaussian, galaxies are treated as a sum of two Gaussians with same ellipticity and position angle.

We use high signal-to-noise unsaturated stars ( $21.5 < r' < 24.5$ ) to map the PSF all over the frame. To make the final catalog, stellar objects with discrepant ellipticity or full width at half maximum (FWHM) were removed through a sigma-clipping procedure. In both images the PSF showed to be nearly constant across the entire field, having an average ellipticity of 4.4% and 6.0% in the  $g'$  and  $r'$  images, respectively.



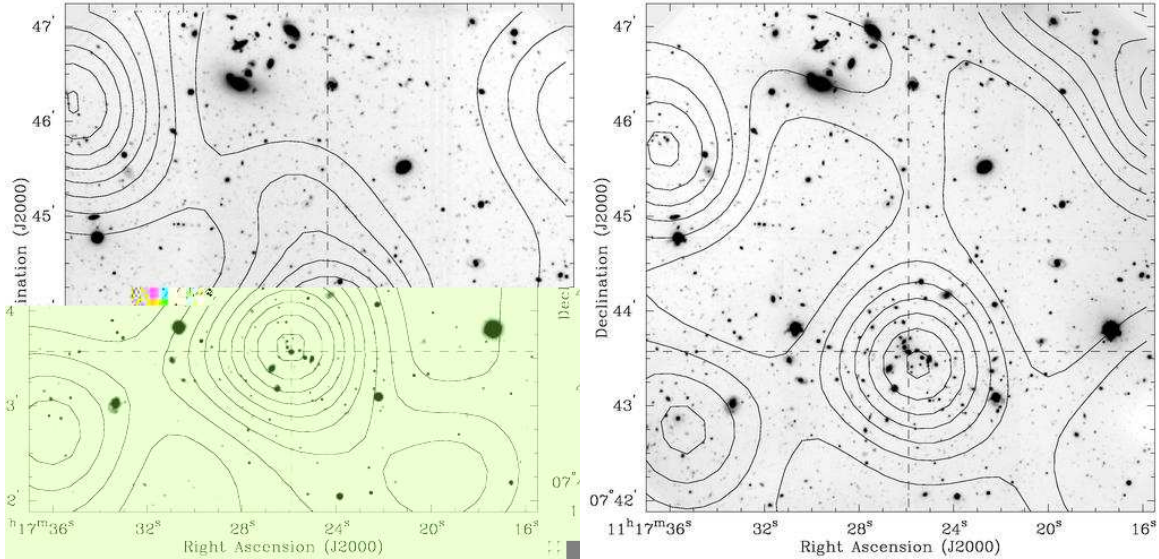


FIG. 8.— Weak-Lensing reconstructed projected mass distributions. *Left panel:* Optical images of [VMF 98] 097 superimposed by constant mass density contours derived from weak shear measurements done over the  $g'$  image. *Right panel:* mass density contours derived from  $r'$  image. The contour levels starts at 4% of  $\Sigma_{\text{crit}}$  (the lensing critical density;  $3 \times 10^3 M_{\odot} \text{pc}^{-2}$  in the present case), and have linear steps of 2%.

To select background galaxies, which are the probes of the weak shear field, we need to rely on their magnitudes and colors to discriminate them from the cluster and/or foreground objects, given that we have not redshift information for the vast majority of them. Ideally we would like to use just galaxies redder than the cluster red-sequence for those objects are supposed to be all behind the cluster (e.g. Broadhurst et al. 2005) but unfortunately, as we can see in Fig. 7, the red-sequence at  $z \sim 0.5$  is very red for this particular combination of filters, and the number of galaxies redder than the red-sequence is too small to provide an adequate sample.

We opt therefore for a simple magnitude and signal-to-noise cut defining the weak lensing sample as all galaxies fainter than  $r'=23.0$  mag ( $M_r = -19.2$  at  $z = 0.485$ ) with ellipticities measured with precision greater than 0.2. This criteria left us with a sample of 1001 (23 gal. arcmin $^{-2}$ ) and 1298 (30 gal. arcmin $^{-2}$ ) galaxies for the  $g'$  and  $r'$  images, respectively with an average magnitude of  $r'=24.9$  mag. By using this criteria we expect some contamination by cluster or foreground galaxies to be present but it should not introduce any bias in the mass reconstruction, only increase the noise.

#### 4.4.2. Surface mass density distribution

The surface mass distribution of the cluster [VMF 98] 097 has been recovered from the shear data using the second version of the LENSENT code (Bridle et al. 1998; Marshall et al. 2002). This algorithm takes the shape of every galaxy image as an independent estimator of the local reduced shear field. The reconstruction of the mass distribution incorporates an intrinsic smoothing whose characteristic scale is determined by Bayesian methods, using a maximum entropy prior. This scale is chosen by maximizing the evidence, given the input data. Using a Gaussian function to smooth the data, we found that its optimal FWHM is  $70''$ .

Figure 8 shows the maps of the reconstructed surface mass density obtained by using data from each of the

images. The maps are very consistent with each other, all showing basically the same features: a main structure clearly associated with the core of [VMF 98] 097, and two smaller structures at the Eastern edge of the field, which can be associated with the E- and NE-structures discussed above. In the  $g'$  map there is a hint of a substructure between the cluster core and the NE-structure. The maps also suggest that there may exist a mass filament joining the E-structure with the main core. In general, it is actually impressive how X-ray emission, surface-mass and galaxy-number densities compare well in this field.

Figure 8 also shows the mass center adopted for the radial analysis presented below (dashed line). This center correspond to one of the brightest red galaxies on the cluster core which is close to the peak of both mass maps, particularly the one reconstructed with the  $g'$  image.

#### 4.5. Mass determination

We now address the measurement of the cluster mass, considering estimates based on weak-lensing of background galaxies and on the ICM X-ray emission.

##### 4.5.1. Weak lensing

For mass estimation through weak-lensing, we opt to use physically motivated mass-density models, to avoid the mass-sheet degeneracy bias (Gorenstein et al. 1988). The two most widely adopted models for fitting shear data are the singular isothermal sphere (SIS) and the NFW profile. The first is a solution of the hydrostatic equilibrium equation for an isothermal self-gravitating system, whereas the second provides a good fit to dark matter halos in numerical simulations (Navarro, Frenk & White 1997).

The SIS profile has the advantage of having a single parameter,  $\sigma$ , which is associated with the line-of-sight velocity dispersion of the galaxies. This density profile is given by:

$$\rho(r) = \frac{\sigma_{cl}^2}{2\pi G r^2} \quad (1)$$

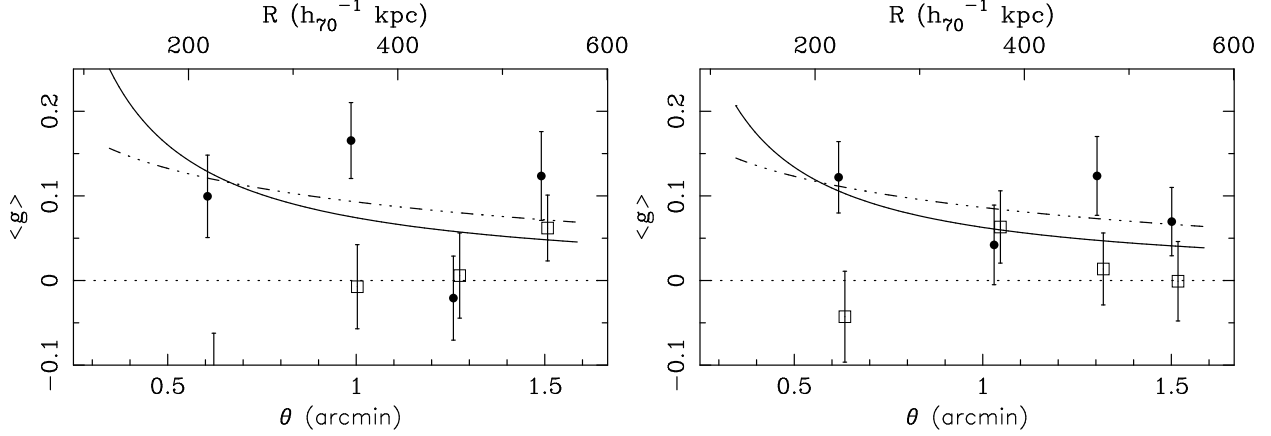


FIG. 9.— Radial profile of the reduced shear  $\langle g \rangle$  for the  $g'$  (left panel) and  $r'$  (right panel). Filled circles represent the average ellipticities of background galaxies, projected tangentially with respect to the cluster center. Each point contains one third of the galaxies ( $\sim 80$ ). The error bars are  $1\sigma$  errors of the mean. Empty squares are the same but for ellipticities projected in a direction  $45^\circ$  with respect to the tangential direction, and should average zero. The solid and the dot-dashed lines represent the best fit of SIS and NFW profiles, respectively.

The NFW profile is described by:

$$\rho(r) = \frac{\rho_c \delta_c}{(r/r_s)(1+r/r_s)^2} \quad (2)$$

where  $\rho_c$  is the critical density,  $r_s$  is a scale radius and  $\delta_c$  is given by

$$\delta_c = \frac{200}{3} \frac{c^3}{\ln(1+c) + c/(1+c)} \quad (3)$$

where  $c$  is the concentration parameter. The approximate virial radius  $R_{200}$  can be defined as  $c \times r_s$ . Lensing formula for the SIS and NFW profiles came from King & Schneider (2001).

These parametric models were fitted to the peak of the mass map corresponding to the cluster core using the procedure described in Cypriano et al. (2004). We restricted the data to the region  $15'' < r < 1'6$  in relation to the mass center showed in Fig. 8. Data points closer to the center have been removed because they correspond to a region where the lensing effects are no longer linear (strong lensing region) and  $1'6$  is the distance to the closest image border. Given these limits, the number of data points included in this analysis is 302 and 373 for the  $g'$  and  $r'$  images, respectively.

The reduced shear (and the derived mass profile parameters) depends on the mean redshift of the background galaxies through the mean value of the ratio  $\beta \equiv D_{ls}/D_s$  of the angular diameter distances between the cluster and the sources and to the sources. We have estimated this quantity for our sample of background galaxies using a catalog of magnitudes and redshifts in the Hubble Deep Field (Fernández-Soto et al. 1999) with both the same bright limit cutoff and the same average magnitude, obtaining in both cases  $\langle \beta \rangle = 0.44$ .

In Fig. 9 we plot the binned data points of the galaxy ellipticities as well as the best fitted SIS and NFW models. The best fitted parameters of these models are presented in Table 1.

Our data poorly constrains the NFW concentration parameter because it controls the variation of the density slope in the very inner ( $r \ll r_s$ ) or outer ( $r > R_{200}$ ) regions, which we do not probe in our weak-lensing analysis. Consequently, we decided to keep the value of  $c$  constant,  $c = 5$ , and fit only  $R_{200}$ .

The results obtained for the  $r'$  and  $g'$  images are fully consistent within the errors. The same is not valid for the two models. The SIS results tend to give smaller values for the cluster mass when compared with the results obtained with the NFW model, because within the restricted radial range we are considering here the SIS profile is steeper than the NFW.

It is worth mentioning that the values of  $R_{200}$  obtained through weak-lensing are significantly above those from the virial analysis presented in Sec. 4.1. We shall come back to this issue in Sec. 5.

#### 4.5.2. X-ray Brightness profiles and mass determination

The gas-density profile is obtained from the radial X-ray surface-brightness profile. We assume that the gas has a number-density profile given by the  $\beta$ -model (Cavaliere & Fusco-Femiano 1976):

$$n(r) = n_0 \left[ 1 + (r/r_c)^2 \right]^{-3\beta/2}, \quad (4)$$

where  $r_c$  is the core radius and  $n_0$  the central number-density of electrons. Then, the X-ray surface-brightness profile is:

$$I(R) = I_0 \left[ 1 + (R/R_c)^2 \right]^{-3\beta+1/2}, \quad (5)$$

assuming that the gas is isothermal and the core radius  $R_c = r_c$  (capital and lowercase symbols refer to 3D and projected quantities, respectively).

The X-ray brightness profile of [VMF 98] 097 was obtained using the STSDAS/IRAF task ELLIPSE, with the sum of the MOS1 images corresponding to observations with obsID 203560201 and 203560401 in the 0.3–8.0 keV energy band. Each image was binned by a factor 128 so that 1 image pixel was  $6''.4$ . The brightness profile was extracted up to  $125''$ , corresponding to  $\sim 750 h_{70}^{-1}$  kpc at the cluster redshift.

Figure 10 shows the cluster core X-ray emission profile together with the best least-squares fitted  $\beta$ -model. We have obtained  $r_c = 21''.1 \pm 0''.9$  ( $127 \pm 5$  kpc) and  $\beta = 0.526 \pm 0.014$ . The central electronic density,  $n_0$ , is estimated using the emission integral,  $EI = \int n_e^2 dV$  (see Sarazin 1988), which is related to the thermal spectrum normalization parameter given by XSPEC. Using

the thermal spectrum extracted within  $66''$ , we have obtained  $n_0 = (3.4 \pm 0.4) \times 10^{-3} \text{ cm}^{-3}$ .

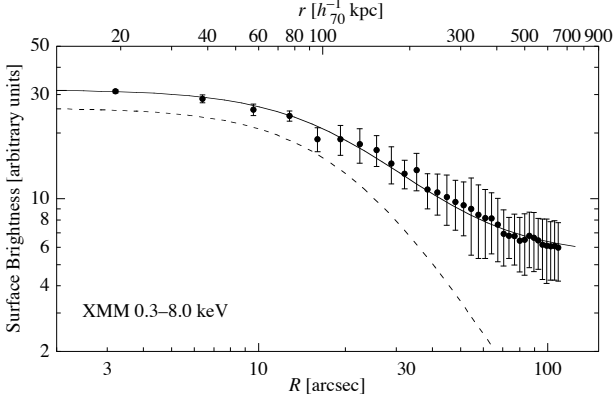


FIG. 10.— X-ray surface brightness profile in the [0.3–8.0 keV] band fitted by a  $\beta$ -model. The full line is the fit to the cluster plus background emission. The dashed line corresponds to the inferred X-ray emissivity of the cluster.

The radial gas-mass profile can be simply obtained by integrating the density profile in concentric spherical shells. The dynamical (total) mass is computed assuming an isothermal gas in hydrostatic equilibrium. Even summing all XMM observations, we have enough counts only to compute a single emission-weighted temperature. Using the temperature previously determined,  $kT = 3.3 \text{ keV}$ , the computed dynamical mass is presented in Fig. 11. At  $r = 125''$ , the total mass inferred from X-rays is  $1.4 \times 10^{14} M_\odot$ .

The gas mass fraction,  $f_{\text{gas}}$ , is computed as the ratio between the gas mass and the total mass at a given radius. This ratio is related to the cluster baryon fraction as  $f_{\text{baryon}} = f_{\text{gas}}(1 + M_{\text{gal}}/M_{\text{gas}})$ , where  $M_{\text{gal}}$  is the baryonic mass in the galaxy cluster members. The baryonic mass in galaxies may be estimated as  $M_{\text{gal}} \approx 0.16 h_{70}^{0.5} M_{\text{gas}}$  (White et al. 1993; Fukugita, Hogan, & Peebles 1998). The bottom panel of Fig. 11 shows the baryon fraction radial profile. At  $r = 125''$ ,  $f_{\text{gas}} = 0.07$ , with a rising trend. The X-ray observations are not deep enough to detect the point where  $f_{\text{gas}}$  flattens, as is observed in several clusters (e.g., Allen, Schmidt & Fabian 2002).

#### 4.5.3. A comparison between weak-lensing and X-ray masses

At a radius of  $0.5 h_{70}^{-1} \text{ Mpc}$ , the inferred weak-lensing masses from the  $r'$  image are  $2.1 \times 10^{14} M_\odot$  and  $3.4 \times 10^{14} M_\odot$  for the SIS and NFW profiles, respectively. At the same radius, the X-ray mass is  $7.0 \times 10^{13} M_\odot$ , i.e. the weak-lensing mass is 3.4 (SIS) to 4.8 (NFW) times the value inferred through the X-ray emission. The possible causes for such discrepancy are given in the next section.

### 5. DISCUSSION

Our results strongly suggest that we are witnessing the mass assembly of a cluster at  $z = 0.485$ . There are several hints pointing towards this suggestion.

The morphology of the cluster is complex, presenting at least two significant substructures. The X-ray emission, the galaxy distribution, and the surface-mass density map, all present the same overall features: the cluster core and the E and NE-structures. The E-structure

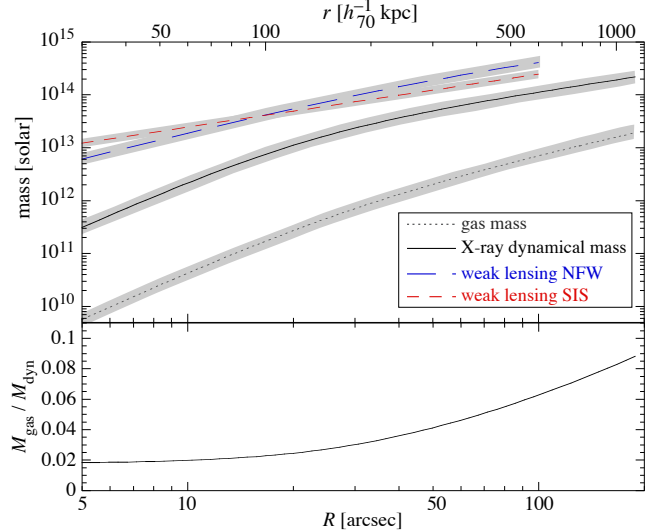


FIG. 11.— *Top panel:* Gas (dotted line) and X-ray dynamical mass (solid line) growth curves derived from the assumed  $\beta$ -model. They are compared to the weak-lensing mass estimated with a SIS (short-dashed line) and NFW (long-dashed line) profiles. The grey regions correspond to  $1\sigma$  statistical errors. *Bottom panel:* Gas mass fraction profile derived using the X-ray data.

and the cluster core have a projected distance less than 1 Mpc (at the cluster redshift) and, as we argued in sections 4.2 and 4.3, are probably at the same redshift. The substructure located between the cluster core and the NE-structure seem in the projected galaxy distribution (Figure 6) might be also real, since there is a feature present in our  $g'$  weak-lensing map close to it.

The velocity distribution of the region is also complex, with multiple peaks in a small redshift range (Fig. 5). The statistical analysis presented in Section 4.1 indicates, for instance, the presence of three velocity-substructures: S1, S2 and S3.

Additional evidence of dynamical activity in clusters can be obtained from its brightest galaxy. For local X-ray luminous groups and poor clusters, the most luminous galaxies (BGGs) lie near the peak of the X-ray emission (e.g. Mulchaey & Zabludoff 1998). However, at intermediate redshift, this picture may be different. A recent study of X-ray groups and poor cluster at moderate redshift by Mulchaey et al. (2006) suggest that the brightest galaxies in groups and poor clusters are still in the process of forming, as late as at  $z \sim 0.2$ , in some systems. The indication is given by the offset between the BGG and the X-ray emission and offsets between the velocity of the BGGs and the mean velocity of the system. This scenario is consistent with recent numerical simulations (De Lucia & Blaizot 2007). In the case of [VMF 98]097, the X-ray emission is associated with the velocity structure S1. This structure has two elliptical galaxies in the center with comparable luminosities: galaxy 947 with  $r' = 20.26 \text{ mag}$ ,  $cz = 145882 \text{ km s}^{-1}$ , and galaxy 1098 with  $r' = 20.29 \text{ mag}$ ,  $cz = 144645 \text{ km s}^{-1}$ . The peak of the X-ray emission is offset by  $\sim 9''$  from both galaxies. Furthermore, the brightest elliptical galaxy (number 947) is offset significantly in velocity from the mean velocity of the structure S1 ( $> 1000 \text{ km s}^{-1}$ ). These results provide additional evidences of an on-going dynamical activity in this cluster.

The mass estimates obtaining using X-rays and

weak-lensing are very discrepant, and this is usually interpreted as evidence of dynamical activity (e.g., Cypriano et al. 2004). In fact, X-ray mass estimates are based on the assumption of hydrostatic equilibrium, which may not hold in the presence of mergers or strong tidal interactions. It also depends on the assumption that the  $\beta$ -model describes well the gas density radial profile.

The accuracy of mass determination based on X-ray observations has been studied through hydrodynamical simulations. Evrard et al. (1996) and Schindler (1996) find that, usually, X-ray estimates are good within 50%, with no systematic bias. In the case of an extreme non-equilibrium clusters, the mass deviation from the true value can be as high as a factor 2. However, more recently, Rasia et al. (2006) conclude that X-ray estimation of the total mass is biased towards lower values when using the  $\beta$ -model if the cluster is not in equilibrium. The typical estimated mass is around 40% of the true mass at about half the virial radius.

Another possibility is that the excess between lensing and X-ray masses (a factor  $\sim 3.6$ ) is due to the intervening mass along the line-of-sight of the cluster, which leads to an over-estimate of the weak-lensing mass of a few tens of percent (Metzler et al. 2001), although this excess seems too high to be due to this effect only. On the other hand, the velocity dispersion in the region of the cluster core is consistent with equilibrium between gas and galaxies (Sect. 4.1).

Based on the color-magnitude analysis presented in Sect. 4.3, it is unlikely that the E-structure is a foreground group. Besides, the E-structure contains two galaxies at the cluster redshift and is detected by weak-lensing mass reconstruction and by X-rays. It lies roughly at  $1 h_{70}^{-1}$  Mpc from the center of [VMF 98] 097 and thus could be a substructure of the cluster.

The NE-structure poses a more challenging problem, since we do not have any galaxy with measured redshift in this region. Nevertheless, it is an overdensity detected in X-rays, in the galaxy projected number density map, and also by weak lensing. This suggests that it should be relatively massive. In order to probe its nature, we have compared their median magnitudes and the color ( $g'-r'$ ) with those of the cluster core and the E-structure. Galaxies in the NE-structure are significantly fainter and bluer and, consequently, we suggest that it is indeed a background cluster, although spectroscopic information is necessary to verify such a claim.

## 6. SUMMARY AND CONCLUSION

We have presented an optical and X-ray based study of [VMF 98] 097 (RX J1117.4+0743), an intermediate mass structure located at  $z=0.485$ . We demonstrate in this work that it is possible to obtain a good weak-lensing data for a distant cluster even with non-exceptional seeing conditions ( $0''.7-0''.8$ ) and with small field of view. Our main results are summarized in the next paragraphs.

The cluster shows a very complex structure. We find that velocity distribution of member galaxies is at least bimodal, with two well defined structures along the line-of-sight. The two main structures, named S1 with 23 galaxies and S2 with 9 galaxies, form the cluster core. These structures have a velocity dispersion of  $592 \pm 82$  km s $^{-1}$  and  $391 \pm 85$  km s $^{-1}$  respectively. Using the projected

density map of 272 galaxies brighter than  $r'=23$  mag we were able to identify several structures in the neighborhood of [VMF 98] 097. These structure are also presented in X-ray and in the weak-lensing maps. The high density regions identified in the maps are: the cluster core formed by S1 and S2, the foreground group RIXOS F258.101 (located  $\sim 2'.5$  North from [VMF 98] 097), and two other overdensities, the E-structure and the NE-structure. We do not have redshift information of the galaxies belonging to these two structures, except for two galaxies at the cluster redshift in the E-structure. Therefore, we have used the median magnitudes and colors of the galaxies inside a  $20''$  radius from the peak of these overdensities to investigate the possibility if these structures are linked to [VMF 98] 097. Based on this analysis and in the detection given by the weak-lensing and X-ray maps (section 4.3) we conclude that the E-structure is a sub-structure associated to the cluster. Using the same approach for NE-structure, we find that the galaxies in the region of this overdensity are significantly fainter and bluer than the galaxies in the cluster core and in the E-structure, suggesting that the NE-structure is a background cluster. However additional spectroscopic observations are necessary to verify this point.

We have used the color-magnitude relation to analyze the galaxy contents in structures S1, S2 and S3. We find that the galaxy populations in S1 and S2+S3 differ in its content. Most of the galaxies in S1 are redder than those presented in S2 and S3, with an average color of  $g'-r' \sim 1.9$ . They lie well inside the red sequence for passive galaxies (see Fig. 7(a)). S2 and S3 are dominated by a population of blue, star-forming galaxies that, in average, are  $\sim 0.3$  mag fainter than the galaxies in S1. Further evidence is provided by the fraction of emission-line galaxies in each of the structure. We find that only 17% of the galaxies in S1 are emission-line galaxies, while the fraction of emission-line galaxies in S2 and S3 is of the order of 31%, in agreement with the galaxy contents derived for both structures from the color-magnitude relation analysis.

We derived the X-ray temperature, the metal abundance and X-ray flux and luminosity in different energy bands using the plasma model described in section 3.1. For the computed intra-cluster medium temperature of  $kT = 3.3_{-0.6}^{+0.7}$  keV we find, using the  $T_X - \sigma$  relation from Xue & Wu (2000), a velocity dispersion of  $\sigma = 672_{-53}^{+57}$  km s $^{-1}$ . This value agrees well with the derived line-of-sight velocity dispersion obtained for S1 ( $592 \pm 82$  km s $^{-1}$ ), suggesting that the X-ray emission is mainly associated to this structure. In addition, we find that the cluster is slightly hotter than expected for its luminosity ( $L_X^{bol} = 11.8 \pm 0.9 \cdot 10^{43} h_{70}^{-2}$  erg s $^{-1}$ ), compared to the local  $L_X - T_X$  correlation. However, its fall right on the sub-sample relation at  $z \approx 0.34$  of Novicki et al. (2002).

We have used the weak-lensing analysis to map the mass distribution in the area of the cluster. We find a good agreement between the velocity dispersions derived from the  $g'$  and  $r'$  using the SIS model profile. However, there is a disagreement with the values obtained from X-ray and from the kinematic of the member galaxies. We used two fit models, the SIS and NFW, to compute the total mass of the cluster. We find that the total mass inferred from weak-lensing of  $2.1$  to  $3.7 \times 10^{14} M_\odot$



at  $r = 0.5h_{70}^{-1}$  Mpc (depending on the band and the model adopted) is well in excess compared to the X-ray mass. However, given the several difficulties for an accurate gravitational lensing estimation in this field, particularly due to the contribution of the other mass clumps and the uncertainty on the average redshift of the background galaxies, these results should be taken with caution. The presence of several sub-structures in the X-ray, weak-lensing mass and galaxy density maps, the existence of a bridge of matter in the center of the cluster connecting different sub-structures (detected in weak-lensing only) and the complex velocity distribution of member galaxies reveal that this cluster is dynamical active. Additional evidence of the dynamical activity is given by the offsets we see between the two brightest galaxies in the cluster core and the X-ray emission and the significantly offset between the velocity of the galaxy 947 (the brightest elliptical galaxy in S1) and the mean velocity of structure S1. Our main conclusion is that this poor cluster may be the core of a still forming rich cluster of galaxies. [VMF 98] 097 is in an environment with other nearby substructures that, given their

projected distance to the cluster, are probably gravitationally bound and will eventually merge to form a rich cluster.

We would like to thank the anonymous referee for the useful comments and suggestions. ERC acknowledges the hospitality of the Departament of Astronomy of the Instituto de Astronomia, Geofísica e Ciências Atmosféricas, Universidade de São Paulo, where this work was partially done. ERC also acknowledges the support from CNPq through the PROSUL project. GBLN, LSJ and CMO acknowledge support by the Brazilian agencies FAPESP and CNPq. We made use of the XMM-Newton archival data: the XMM-Newton is an ESA Science Mission with instruments and contribution directly funded by ESA member states and the USA (NASA) and the NASA/IPAC Extragalactic Database (NED) which is operated by the Jet Propulsion Laboratory, California Institute of Technology, under contract with the National Aeronautics and Space Administration.

## REFERENCES

- Allen, S.W., Schmidt, R., & Fabian, A.C. 2002, *MNRAS*, 334, L11
- Ashman, K. M., Bird, C. M. & Zepf, S. E. 1994, *AJ*, 106, 2348
- Bahcall, N. A. 1979, *ApJ*, 232, 689
- Balogh, M., Bower, R. G., Smail, I., Ziegler, B. L., Davies, R. L., Gaztelu, A., Fritz, A., 2002, *MNRAS*, 337, 256
- Balucinska-Church, M. & McCammon D. 1992, *ApJ*, 400, 699
- Bertin, E. & Arnouts, S. 1996, *A&AS*, 117, 393
- Beers, T. C., Flynn, K. & Gebhardt, K. 1990, *AJ*, 100, 32
- Bridle, S. L., Hobson, M. P., Lasenby, A. N. & Saunders, R. 1998, *MNRAS*, 299, 895
- Bridle, S., Kneib, J.-P., Bardeau, S., Gull, S.F., 2002, in “The shapes of Galaxies and their Dark Halos” Yale Cosmology workshop, 28-30 May 2001, World Scientific.
- Broadhurst, T., Takada, M., Umetsu, K., Kong, X., Arimoto, N., Chiba, M., & Futamase, T. 2005, *ApJ*, 619, L143
- Burns, J. O., Loken, C., Roettiger, K., Rizza, E., Bryan, G., Norman, M. L., Gómez, P., Owen, F. N., 2002, *New Astronomy Reviews*, 46, 135
- Carlberg, R. G., Yee, H. K. C., Ellingson, E., Abraham, R., Gravel, P., Morris, S. & Pritchet, C. J. 1996, *ApJ*, 462, 32
- Carlberg, R. G., Yee, H. K. C., Morris, S. L., Lin, H., Hall, P. B., Patton, D. R., Sawicki, M., Shepherd, C. W., 2001, *ApJ*, 552, 427
- Cardelli, J. A., Clayton, G. C. & Mathis, J. S. 1989, *ApJ*, 345, 245
- Cavaliere A. & Fusco-Femiano R., 1976, *A&A* 49, 137
- Colberg, J. M., White, S. D. M., Jenkins A. & Pearce, F. R. 1999, *MNRAS*, 308, 593
- Cypriano, E. S., Sodr   Jr., L., Kneib, J.-P. & Campusano, L. E. 2004, *ApJ*, 613, 95
- Cypriano, E. S., Lima Neto, G. B., Sodr   Jr., L., Kneib, J.-P. & Campusano, L. E. 2005, *ApJ*, 630, 38
- De Lucia, G. & Blaizot, J. 2007, *MNRAS*, 375, 2
- Dickey J.M., Lockman F.J. 1990, *Ann. Rev. Ast. Astr.* 28, 215
- Dressler, A., Oemler, A., Jr., Couch, W. J., Smail, I., Ellis, R. S., Barger, A., Butcher, H., Poggianti, B. M., Sharples, R. M., 1997, *ApJ*, 490, 577
- Ehle, M., Breitfellner, M., Gonzalez Riestra, R., Guainazzi, M., Loiseau, N., Rodriguez, P., Santos-Lles, M., Schartel, N., Tomas, L., Verdugo, E. & Dahlem, M. 2006, “XMM-Newton Users’ Handbook”, Issue 2.4
- Evrard, A. E., Metzler, C. A., Navarro, J. F., 1996, *ApJ*, 469, 494
- Fahlman, G., Kaiser, N., Squires, G. & Woods, D. 1994, *ApJ*, 437, 56
- Fern  ndez-Soto, A., Lanzetta, K.M., & Yahil, A. 1999, *ApJ*, 513, 34
- Ferrari, C., Benoist, C., Maurogordato, S., Cappi, A. & Slezak, E. 2005, *A&A*, 430, 19
- Fukugita, M., Ichikawa, T., Gunn, J. E., Doi, M., Shimasaku, K. & Schneider, D. P. 1996, *AJ*, 111, 1748
- Fukugita, M., Hogan, C.J., & Peebles, P.J.E. 1998, *ApJ*, 503, 518
- Gilbank, D. G., Bower, R. G., Castander, F. J., Ziegler, B. L., 2004, *MNRAS*, 348, 551
- Gomez, P. L., Pinkney, J., Burns, J. O., Wang, Q., Owen, F. N., Voges, W., 1997, *ApJ*, 474, 580
- Gonzalez, A. H., Tran, K. V., Conbere, M. N. & Zritsky, D. 2005, *ApJ*, 624, L73
- Gorenstein, M.V. Falco, E.E. & Shapiro, I.I. 1988 *ApJ*, 327, 693
- Heisler, J., Tremaine, S. & Bahcall, J. N. 1985, *ApJ*, 298, 8
- Holden, B. P., Stanford, S. A., Eisenhardt, P., Dickinson, M., 2004, *AJ*, 127, 2484
- Hook, I., J  rgensen, I., Allington-Smith, J. R., Davies, R. L., Metcalfe, N., Murowinski, R. G., Crampton, D. 2004, *PASP*, 116, 425
- Jeltema, T.E., Mulchaey, J.S., Lubin L.M., Rosati P., Bohringer H., 2006, *ApJ*, 649, 649
- Jenkins, A., Frenk, C. S., Pearce, F. R., Thomas, P. A., Colberg, J. M., White, S. D. M., Couchman, H. M. P., Peacock, J. A., Efstathiou, G., Nelson, A. H., 1998, *ApJ*, 499, 20
- Kaasra, J.S., Mewe, R. 1993, *A&A Suppl.* 97, 443
- King, L. J. & Schneider, P. 2001, *A&A*, 369, 1
- Landolt, A.U. 1992, *AJ*, 104, 340
- Liedahl, Duane A., Osterheld, Albert L., Goldstein, William H. 1995, *ApJ*, 438, L115
- Lima Neto, G. B., Capelato, H. V., Sodr  , L., Jr. & Proust, D. 2003, *A&A*, 398, 31
- Marshall, P. J., Hobson, M. P., Gull, S. F., Bridle, S. L. 2002, *MNRAS*, 335, 1037
- Mason, K. O., et al. 2000, *MNRAS*, 311, 456
- Metzler, C. A., White, M., Loken, C., 2001, *ApJ*, 547, 560
- Mulchaey, J. S. & Zabludoff, A. I. 1998, *ApJ*, 496, 73
- Mulchaey, J. S., Lubin, L. M., Fassnacht, C., Rosati, P. & Jeltema, T. E. 2006, *ApJ*, 646, 133
- Mullis et al. 2003, *ApJ*, 594, 154
- Navarro, J. F., Frenk, C. S. & White, S. D. M. 1997, *ApJ*, 490, 493
- Novicki M.C., Sornig M., Henry J.P., 2002, *AJ* 124, 2413
- Oemler, A., Jr., Dressler, A., Butcher, H. R., 1997, *ApJ*, 474, 561
- Pell  , R., Sanahuja, B., Le Borgne, J. F., Soucail, G. & Mellier, Y. 1991, *ApJ*, 366, 405.
- Pierre, M., Soucail, G., Boehringer, H. & Sauvageot, J. L. 1994, *A&A*, 289, L37
- Ramella, M., Zamorani, G., Zucca, E., Stirpe, G. M., Vettolani, G., Balkowski, C., Blanchard, A., Cappi, A., 1999, 342, 1
- Rasia, E., Ettori, S., Moscardini, L., Mazzotta, P., Borgani, S., Dolag, K., Tormen, G., Cheng, L. M., Diaferio, A., 2006, *MNRAS*, 369, 1013
- Richstone, D., Loeb, A., Turner, E. L., 1992, *ApJ*, 393, 477
- Roettiger, K., Burns, J. O., Loken, C., 1996, *ApJ*, 473, 651

- Sarazin C.L., 1988, "X-ray emission from clusters of galaxies", Cambridge Univ. Press
- Schindler, S., 1996, A&A 305, 756
- Schlegel, D. J., Finkbeiner, D. P. & Davis, M. 1998, ApJ, 500, 525
- Silverman,, B. W., 1986
- Smail, I., Dressler, A., Couch, W. J., Ellis, R. S., Oemler, A., Jr., Butcher, H., Sharples, R. M., 1997, ApJSupp., 110, 213
- Tonry, J., Davis, M. 1979, AJ, 84, 1511
- van Dokkum, P. G., Franx, M., Kelson, D. D., Illingworth, G. D., Fisher, D., Fabricant, D. 1998, ApJ, 500, 714
- Vikhlinin, A. et al. 1998, ApJ, 502, 558
- Willis, J.P., Pacaud, F., Valtchanov, I. et al., 2005, MNRAS, 363, 675
- Wilman, D. J., Balogh, M. L., Bower, R. G., Mulchaey, J. S., Oemler, A., Carlberg, R. G., Morris, S. L., Whitaker, R. J., 2005, MNRAS 358, 71
- West, M. 1991, ApJ, 379, 19
- White, S.D.M., Navarro, J.F., Evrard, A.E., & Frenk, C.S. 1993, Nature, 366, 429
- Xue, Y.J. & Wu, X.P., 2000, ApJ, 538, 65

TABLE 1  
GALAXY RADIAL VELOCITIES CATALOG

Galaxy id	RA(2000)	DEC(2000)	$r_0^{(c)}$ (mag)	$(g' - r_0^{(c)})$ (mag)	$V_{hel}$ (km s <sup>-1</sup> )	$\delta v$ (km s <sup>-1</sup> )	R	#lines
514	11 17 18.76	+07 42 42.3	20.49	1.98	183007	84	3.39	...
2492	11 17 19.55	+07 46 01.0	22.63	1.28	143704	36	4.27	...
1937	11 17 19.36	+07 45 07.7	19.41	0.94	109039	36	...	8
202	11 17 19.35	+07 46 18.9	19.85	0.91	68022	10	...	9
21	11 17 19.76	+07 47 03.2	19.11	1.46	107761	45	3.72	...
1520	11 17 19.59	+07 44 30.5	19.12	1.58	99787	40	9.06	...
2079	11 17 21.80	+07 45 18.4	22.56	0.98	144968	10	...	8
2315	11 17 21.73	+07 45 41.8	22.42	0.71	70683	59	...	10
676	11 17 22.40	+07 43 11.2	20.79	1.86	147672	61	4.60	...
918	11 17 22.37	+07 43 22.4	20.35	1.90	144136	61	5.12	...
2691	11 17 22.81	+07 46 23.4	21.25	1.46	170804	42	3.83	...
1	11 17 22.69	+07 45 31.4	17.11	1.09	38300	34	...	6
2572	11 17 23.04	+07 46 06.2	21.98	1.54	155596	35	4.81	...
1570	11 17 23.02	+07 44 35.3	21.19	1.32	144939	48	2.57	...
1576	11 17 23.00	+07 44 40.2	21.48	1.60	143740	46	3.70	...
1568	11 17 23.29	+07 44 31.9	21.36	1.68	143192	45	...	8
135	11 17 23.44	+07 46 36.5	20.73	1.75	202462	41	3.77	...
2131	11 17 23.95	+07 45 23.3	21.57	1.42	141945	52	4.75	...
1299	11 17 24.29	+07 44 10.6	19.65	1.72	147286	39	6.91	...
190	11 17 24.14	+07 46 40.8	20.94	1.15	103336	23	8	...
694	11 17 24.48	+07 42 58.2	21.53	1.94	144522	57	7.26	...
3054	11 17 24.47	+07 42 13.7	22.16	1.82	148235	61	4.57	...
339	11 17 24.80	+07 42 24.3	22.48	1.13	105922	13	...	8
739	11 17 24.61	+07 43 04.5	21.83	0.86	93069	20	...	13
908	11 17 25.05	+07 43 29.7	19.26	1.66	147157	48	4.23	...
2973	11 17 25.22	+07 42 04.6	20.46	1.94	145243	42	7.25	...
441	11 17 25.54	+07 42 34.0	22.37	0.91	146836	24	...	8
910	11 17 25.92	+07 43 34.5	19.80	0.92	90311	12	...	15
1085	11 17 25.86	+07 43 43.1	20.83	1.96	145337	56	5.35	...
903	11 17 26.14	+07 43 53.3	20.64	1.89	146283	39	8.36	...
2156	11 17 26.14	+07 45 29.7	20.59	1.88	145026	38	8.47	...
1098	11 17 26.12	+07 43 41.0	20.29	1.84	144645	49	5.36	...
947	11 17 26.09	+07 43 37.5	20.26	1.94	145882	47	6.11	...
1205	11 17 26.48	+07 43 53.1	22.10	1.23	149339	30	5.16	...
1269	11 17 26.45	+07 44 02.7	21.25	1.98	144528	24	7.79	...
2346	11 17 26.28	+07 45 48.3	20.99	1.32	103397	72	...	10
904	11 17 26.75	+07 43 24.0	18.90	0.94	48309	10	...	10
1268	11 17 26.58	+07 44 07.6	22.21	1.14	103535	26	...	6
798	11 17 26.52	+07 43 11.3	19.73	1.29	144724	44	7.50	...
623	11 17 26.83	+07 42 51.6	20.77	1.96	147448	57	6.08	...
1939	11 17 26.79	+07 45 08.1	20.88	1.77	170714	49	3.10	...
1538	11 17 27.47	+07 44 28.5	21.48	1.81	143797	51	5.85	...
1153	11 17 27.46	+07 43 50.1	21.18	1.86	183716	28	4.74	...
10	11 17 27.45	+07 46 57.2	17.57	1.30	47253	45	9.84	...
121	11 17 27.42	+07 46 47.7	19.15	1.27	47925	45	8.76	...
1241	11 17 27.58	+07 44 00.0	21.54	1.45	145443	21	7.72	...
545	11 17 27.76	+07 42 45.1	20.70	1.94	143211	50	9.12	...
510	11 17 27.73	+07 42 38.4	22.57	1.16	148356	76	3.94	...
3	11 17 28.36	+07 46 36.6	18.10	1.27	47375	29	11.94	...
95	11 17 28.92	+07 46 55.2	20.58	0.59	65862	15	...	12
1611	11 17 29.06	+07 44 37.3	21.46	1.12	149186	56	...	8
1071	11 17 29.31	+07 43 37.6	20.68	1.90	144779	18	12.24	...
2422	11 17 29.22	+07 45 52.1	21.09	1.89	149896	42	7.96	...
2228	11 17 29.55	+07 45 33.9	21.62	1.14	143249	64	4.05	...
7	11 17 29.68	+07 46 48.5	18.09	0.78	40722	10	...	11
5	11 17 29.67	+07 46 23.7	16.65	1.26	47854	43	8.03	...
6	11 17 30.08	+07 46 28.2	18.65	1.14	48516	26	8.75	...
865	11 17 30.03	+07 43 16.2	22.12	0.82	65836	25	...	12
24	11 17 30.01	+07 47 06.2	20.12	0.71	48649	18	...	10
325	11 17 30.28	+07 42 13.1	22.43	0.99	146910	26	4.18	...
2105	11 17 30.19	+07 45 23.3	20.27	1.28	149665	48	4.20	...
1372	11 17 30.56	+07 44 13.4	22.12	1.18	157677	19	...	9
864	11 17 30.50	+07 43 16.6	20.10	1.56	154346	40	6.53	...
1099	11 17 30.42	+07 44 04.2	20.51	1.89	144382	37	7.69	...
2571	11 17 31.07	+07 46 10.3	21.25	1.49	47531	56	3.29	...
988	11 17 30.99	+07 43 29.6	19.70	1.04	107733	64	...	8
1793	11 17 30.86	+07 44 52.4	21.89	0.56	300960	114	...	7
2921	11 17 31.82	+07 41 57.9	21.21	2.01	153491	50	5.12	...
1811	11 17 32.28	+07 44 55.3	21.14	1.80	157625	32	6.60	...
1219	11 17 32.42	+07 43 58.0	21.66	1.94	145199	44	6.52	...
663	11 17 33.43	+07 43 01.3	18.79	0.41	12677	16	...	13
525	11 17 34.31	+07 42 40.0	22.30	1.92	184040	57	4.91	...
359	11 17 35.53	+07 42 29.2	21.30	1.47	147726	60	3.62	...
313	11 17 35.73	+07 42 52.6	19.99	1.98	143826	35	5.80	...
1719	11 17 35.89	+07 44 59.7	19.33	0.68	33815	41	...	12

NOTE. — The units of Right Ascension are hours, minutes and seconds, and those of Declination are degrees, arcminutes and arcseconds.

TABLE 2  
SUMMARY OF XMM OBSERVATIONS.

obs. date	obsID	detector	net exp. time (ks)	net counts
2001-11-25	082340101	MOS1	47.5	252
2001-11-25	082340101	PN	40.3	611
2004-06-10	203560201	MOS1	59.2	322
2004-06-26	203560401	MOS1	63.8	389

TABLE 3  
X-RAY FLUX AND LUMINOSITIES IN DIFFERENT ENERGY BANDS (IN  
KEV).

Flux		Luminosity		bolom.
[0.5–2.0]	[2.0–10.0]	[0.5–2.0]	[2.0–10.0]	
$5.25 \pm 0.43$	$3.61 \pm 0.30$	$4.19 \pm 0.35$	$4.44 \pm 0.37$	$11.8 \pm 0.9$

NOTE. — Flux is in units of  $10^{-14} \text{ erg s}^{-1} \text{ cm}^{-2}$ . Luminosity, measured in the source rest frame, is in units of  $10^{43} h_{70}^{-2} \text{ erg s}^{-1}$ .

TABLE 4  
DYNAMICAL PARAMETERS OF THE [VMF 98] 097 STRUCTURES

Structure	RA(2000)	DEC(2000)	$N_{\text{mem}}$	$C_{\text{BI}}$ ( $\text{km s}^{-1}$ )	$S_{\text{BI}}$ ( $\text{km s}^{-1}$ )	$R_{\text{vir}}$ ( $h_{70}^{-1} \text{ Mpc}$ )	$M_{\text{vir}}$ ( $10^{14} M_{\odot} h_{70}^{-1}$ )
S1	11 17 26.4	+07 44 01.3	23	$0.48218 \pm 0.00042$	$592 \pm 82$	$1.02^{+0.13}_{-0.12}$	$1.05^{+0.23}_{-0.10}$
S2	11 17 26.8	+07 42 52.4	9	$0.49191 \pm 0.00048$	$391 \pm 85$	...	...

TABLE 5  
MEDIAN MAGNITUDES AND COLORS OF THE MAIN OVERDENSITY REGIONS IN  
[VMF 98] 097 CLUSTER

Overdensity	# of galaxies	$\langle r' \rangle (R \leq 20'')$ (mag)	$\langle (g' - r') \rangle (R \leq 20'')$ (mag)
cluster core	14	20.67	1.64
E-structure	11	21.81	1.51
NE-structure	7	22.25	1.11

TABLE 6  
MODEL FITTING OF THE WEAK-LENSING DATA.

(1) Method	(2) Filter	(3) Fitted Parameters	(4) $M(r < 0.5 \text{ Mpc})$ ( $10^{14} M_{\odot} h_{70}^{-1}$ )
SIS	$g'$	$\sigma = 809 \pm 89 \text{ km s}^{-1}$	$2.4 \pm 0.5$
SIS	$r'$	$\sigma = 746 \pm 86 \text{ km s}^{-1}$	$2.1 \pm 0.4$
NFW( $c = 5$ )	$g'$	$R_{200} = 2.6 \pm 0.4 \text{ Mpc}$	$3.7 \pm 0.4$
NFW( $c = 5$ )	$r'$	$R_{200} = 2.4 \pm 0.3 \text{ Mpc}$	$3.4 \pm 0.4$